

# 12 Simulating Large Networks of Neurons

Alexander D. Protopapas, Michael Vanier, and James M. Bower

## 12.1 Introduction

The behavior of the nervous system is the outcome of processes at multiple levels of organization. Learning mechanisms, for example, are most likely manifested at all levels from gene expression to synaptic plasticity to changes in behavior. Thus large numbers of neurobiologists interested in learning focus their efforts on the molecular level, while others focus on the single cell, the network, the system, and behavioral levels (Baudry and Davis 1994).

Although investigations at specific levels of scale provide important information about brain organization, it is likely that a complete understanding of the functional organization of the nervous system will require connecting these levels. It is our contention that computer models will increasingly allow us to make just such connections. Indeed, models based on the real anatomy and physiology of the nervous system already constitute what is, in effect, a compact and self-correcting database of neurobiological facts and functional relationships (Bower 1996). We believe that, more and more, laboratories and researchers will rely on such models and modeling software to check the significance and accuracy of their data as well as to further collaboration and communication within neuroscience as a whole.

This chapter serves to document the iterative, multilevel modeling approach we have taken in investigating the functional organization of the mammalian olfactory system. Our work, which started with a network-level simulation of the olfactory, or piriform, cortex originally constructed by Matt Wilson (Wilson and Bower 1992), led to numerous questions regarding the effects of network dynamics on more physiologically realistic cells. Because the original network simulations were based on quite simplified neurons, pursuing this new direction required that we construct much more detailed single-cell simulations, which can then provide a means of upgrading the realism of the cells in the network simulation. In the final section of the chapter, we describe the approach we have taken to improve the network simulation based on the single-cell model.

## 12.2 General Issues

### 12.2.1 The GENESIS Neural Simulator

The models described in this chapter were all generated using the GENESIS neural simulator developed in our laboratory (Wilson et al. 1989) and specifically designed to

allow modeling at many different levels of neural organization (Bower and Beeman 1995). Although other simulation systems support the construction of models at one or another level (see De Schutter 1992), GENESIS remains one of the few that, in principle, support all levels. For example, GENESIS-based models currently exist at the systems (Morissette 1996), network (Wilson and Bower 1989), single-cell (Jaeger, De Schutter, and Bower 1997), and subcellular (Bhalla 1997) levels. A number of key GENESIS features as well as some of the mathematical methods utilized by GENESIS are discussed in appendixes A–E. Additional information about GENESIS can be obtained on the World Wide Web at <http://www.bbb.caltech.edu/GENESIS>. This site also contains a tutorial based on the network simulation described in this chapter (tutorial name: “piriform”) which can be downloaded.

### 12.2.2 Realistic Modeling and Questions of Scale

Our models are all of the sort we have referred to previously as “realistic” (Bower 1990), namely, models primarily based on the actual anatomy and physiology of the nervous system and designed to discover as yet unknown relationships between the structure of the nervous system and its function. *Realistic models* can be contrasted with what we have termed *demonstration models*, which are primarily intended to provide support for a particular preexisting theory or functional point of view. While most theoretical models published to date are of the demonstration type, it is our view that realistic models will become increasingly prominent because they have the greatest chance of discovering new functional relationships. Typically, realistic models are also more closely linked to experimentally testable predictions and therefore of greater use in guiding experimental efforts.

One question that immediately arises in realistic modeling concerns which data to include and which to leave out; this will be specifically addressed in several sections below. In general, however, because realistic models are specifically intended to discover function from structure, they should contain more rather than less biological detail. In addition, the more realistic the model, the more likely it will generate realistic physiological data for comparison with real experiments.

While, in principle, realistic models should include as much biological detail as possible, in practice, there are often real-world limitations on what can be included. The most obvious limitation is computing resources, especially in the case of network modeling, where even complex single-cell models can tax the most sophisticated computers (De Schutter and Bower 1994a, 1994b).

A second, and perhaps more important, limitation on model complexity is the lack of available biological data. Realistic modelers usually discover during the initial stage of model construction that there are large gaps in the information necessary to

construct a model. Although identifying such gaps can serve as a valuable means of directing experimental investigation, the lack of quantitative data often means that information must either be imported from another system, included as a best guess, or excluded from the model altogether.

Finally, the complexity of a model is also a matter of scale and objectives. For example, if the purpose of a network model is to understand the oscillatory structure of the electroencephalogram (EEG), it is both impractical and probably unnecessary to simulate the three-dimensional diffusion of calcium within the network's neurons. Accordingly, all modeling efforts involve some level of abstraction and require initial decisions regarding the level of detail to include in the model. Yet despite the necessity of this type of abstraction, one almost inevitably finds that a model generated at one level of scale raises questions that can only be addressed at another level.

### 12.2.3 The Piriform Cortex Network Model

We developed our modeling methods in the course of our ongoing efforts to understand the mammalian olfactory system (Bower 1995b). Because these methods can be understood only in the context of scientific objectives, we must briefly describe the scientific motivation for our work.

The basis of our first modeling efforts (and of this chapter) is a network model of the piriform cortex constructed several years ago by Matthew Wilson in our laboratory (Wilson and Bower 1989, 1992; Wilson 1990). Piriform cortex is the largest region of primary olfactory cortex and is assumed to be directly involved in olfactory object recognition (Haberly and Bower 1989). Figure 12.1 shows the piriform cortex in the context of the rest of the olfactory system. Odorants arrive at the nasal epithelium, where they activate olfactory receptor neurons. These cells send their axons to the olfactory bulb, which in turn connects to the piriform cortex via the lateral olfactory tract (LOT). The LOT then sends collateral fibers into the piriform cortex, which projects to the entorhinal cortex, which then feeds into the hippocampus,

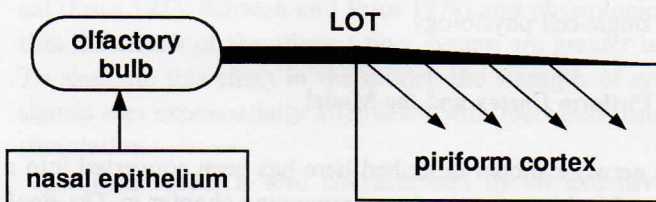


**Figure 12.1**  
Olfactory input to the piriform cortex.

believed to be involved in long-term memory. This is likely to account for the powerful memory-evoking effect of olfactory stimuli (Eichenbaum et al. 1991).

### 12.3 Modeling Objectives

Our ultimate interest in modeling the olfactory cortex is to understand how the piriform cortex network supports the process of olfactory object recognition (Wilson and Bower 1989, Hasselmo et al. 1990). Because our modeling philosophy is to let the structure of the brain tell us something about its function, in constructing realistic models we first identify some physiological feature of the structure to be modeled that is not obviously related to the function of interest, but that can be used to tune model parameters (Bower 1995a, 1996). This exercise builds confidence in the overall structure of the model and also assures us that the model is generating realistic physiological responses for later comparisons to experimental data; it is far more satisfying and reassuring if the model generates interesting behavior without being specifically tuned to do so. In general, we prefer that the functional properties of interest be an emergent property of the simulation rather than a built-in feature.

In the case of the piriform cortex network model, we (M. A. Wilson and J. M. Bower) first focused on replicating the spatial and temporal patterns of activity evoked by artificially stimulating the primary afferent pathway to this network, the lateral olfactory tract (LOT). Evoked potential responses to LOT stimulation are well described (Ketchum and Haberly 1993a) and characteristic of this cortex. Having established the appropriate response patterns to this artificial stimulus, we froze our model parameters and provided a more realistic LOT stimulus. We wanted to determine whether a model tuned on evoked potentials could generate the principal features of the electroencephalogram (EEG), which had been well described previously (Freeman 1960). As demonstrated in later sections, we found that this was the case. Furthermore, the cellular mechanisms revealed by the model to underlie the EEG patterns suggested several novel ideas concerning the functional implications of this network-level behavior for single-cell physiology.

### 12.4 Overall Structure of Piriform Cortex and the Model

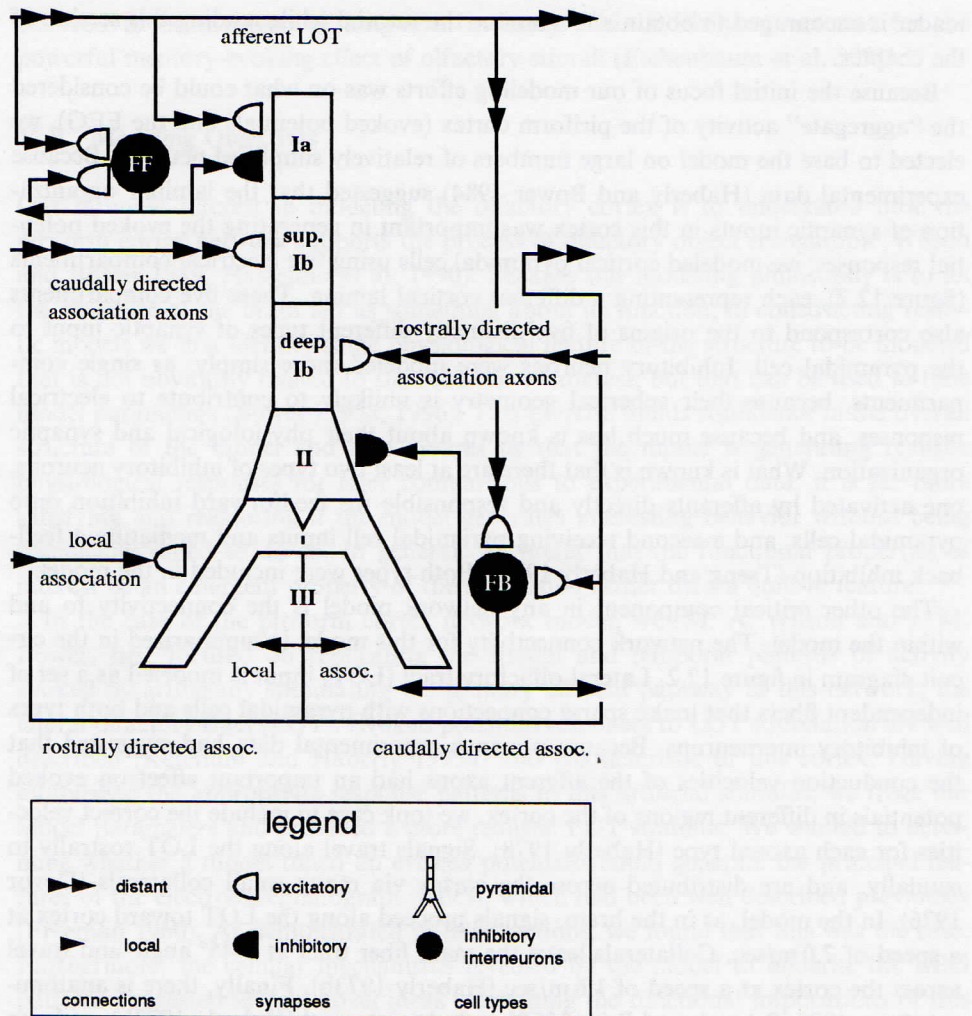
A simplified version of the network model described here has been converted into a computer tutorial with a graphical interface and accompanying chapter in *The Book of GENESIS* (Protopapas and Bower 1995). The tutorial is freely available as part of the standard GENESIS release through <http://www.bbb.caltech.edu/GENESIS>. The

reader is encouraged to obtain and examine the tutorial while reading this section of the chapter.

Because the initial focus of our modeling efforts was on what could be considered the “aggregate” activity of the piriform cortex (evoked potentials and the EEG), we elected to base the model on large numbers of relatively simplified neurons. Because experimental data (Haberly and Bower 1984) suggested that the laminar organization of synaptic inputs in this cortex was important in generating the evoked potential responses, we modeled cortical pyramidal cells using five electrical compartments (figure 12.2), each representing a different cortical lamina. These five compartments also correspond to the origins of five distinctly different types of synaptic input to the pyramidal cell. Inhibitory neurons were modeled more simply, as single compartments, because their spherical geometry is unlikely to contribute to electrical responses, and because much less is known about their physiological and synaptic organization. What is known is that there are at least two types of inhibitory neurons, one activated by afferents directly and responsible for feedforward inhibition onto pyramidal cells, and a second receiving pyramidal cell inputs and mediating a feedback inhibition (Tseng and Haberly 1988). Both types were included in the model.

The other critical component in any network model is the connectivity to and within the model. The network connectivity for this model is summarized in the circuit diagram in figure 12.2. Lateral olfactory tract (LOT) input is modeled as a set of independent fibers that make sparse connections with pyramidal cells and both types of inhibitory interneurons. Because previous experimental data had suggested that the conduction velocities of the afferent axons had an important effect on evoked potentials in different regions of the cortex, we took care to include the correct velocities for each axonal type (Haberly 1978). Signals travel along the LOT rostrally to caudally, and are distributed across the cortex via many small collaterals (Devor 1976). In the model, as in the brain, signals proceed along the LOT toward cortex at a speed of 7.0 m/sec. Collaterals leave the main fiber tract at a 45° angle and travel across the cortex at a speed of 1.6 m/sec (Haberly 1973b). Finally, there is anatomical (Price 1973; Schwob and Price 1978) and physiological (Haberly 1973b) evidence that the effects of the afferent fiber system are greater in rostral than caudal cortex. To simulate this effect in the model, the strength of synaptic input due to afferent signals was exponentially attenuated with increased distance from the rostral site of stimulation.

Piriform cortex is also characterized by an extensive set of intrinsic excitatory connections originating in its own pyramidal cells (Luskin and Price 1983). Physiological data suggested that these intrinsic axonal connections made an important contribution to evoked potentials (Haberly and Bower 1984). These so-called

**Figure 12.2**

Schematic diagram of pyramidal cell and network circuitry. The pyramidal cell consists of five distinct electrical compartments. FF and FB label feedforward and feedback inhibitory cells, respectively. Pyramidal cell axons originate in the layer II (somatic) compartment of the cell. Different compartments are labeled by their layer (Ia, superficial Ib, etc.). The legend explains the symbols in the schematic.

association fibers terminate on the layer-Ib compartments of the pyramidal cells, with the superficial Ib compartment acting as a termination point for caudally directed axons from rostral pyramidal cells in the network. Input from the rostrally directed axons of caudal pyramidal cell is located in deep Ib compartments. Fibers appear to spread out radially from the originating cell and travel rostrally at a speed of 1.0 m/sec, and caudally at a speed of 0.5 m/sec (Haberly 1973b, 1978). Local connections are made on the basal dendrite (Haberly and Presto 1986). These conduction velocities are used in the model to calculate axonal delays. Simulation scaling considerations additionally require that association fiber interconnectivity be greatly increased as compared to that of the actual cortex. As with afferent input, intrinsic excitatory connections are attenuated exponentially with distance from the originating cell.

In general, the pattern of inputs to and outputs from inhibitory neurons is much less well understood biologically. In this model, feedforward inhibitory neurons are activated primarily by the afferent pathway (with some feedback from pyramidal cells) and then form synapses on the Ia compartment of the pyramidal neuron. In contrast, the feedback inhibitory interneurons are activated primarily by pyramidal cell axons (with minor feedforward activation) and form synapses on the somata (layer II) of the pyramidal neuron. Feedforward inhibition is a slow  $\text{GABA}_B \text{ K}^+$ -mediated conductance while feedback inhibition is a fast  $\text{GABA}_A \text{ Cl}^-$ -mediated conductance. Support for the inhibitory architecture of the model comes from a variety of experimental sources (Biedenbach and Stevens 1969a, 1969b; Haberly 1973a; Satou et al. 1982; Haberly and Bower 1984; Tseng and Haberly 1986).

## 12.5 Simplifying Network Components

We have shown how the structure of our model resembles the general structure of the olfactory cortex, and how model components were included in accordance with our initial objective: to generate the evoked potential and EEG response patterns seen in the real cortex. Many specific decisions remain to be made before our model can actually generate output. Indeed, a distinct advantage of constructing realistic models is that you are forced to confront the details, although, as we shall see in the next section, you are also forced to reduce the number of details, or to guess about details for which no biological data are yet available.

### 12.5.1 Connections between Individual Neurons

Having sketched out in general terms the circuitry of our piriform cortex network model, we need to formulate rules that determine the connections between individual

neurons. In the biological network, connections are determined by complex rules for self-organization, which determine the extent of connections and the strength of individual synapses, and which have been shown to be governed by a variety of factors ranging from growth factors to activity-dependent synaptic modification (Purves and Lichtman 1985). Because the biological details for these processes in the piriform cortex are not well understood, the model's network connections were established to conform to general anatomical constraints, but may not necessarily reflect the precise structure of the biological network. Thus, our initial focus on the reconstruction of aggregate electrical activity allowed us to ignore the details of biological connectivity. As our future modeling efforts expand to include learning and memory, we will have to become more concerned with precise patterns of neural interconnectivity.

Since we do not know the biological rules that determine precise connections, we have formulated statistical rules that are within reasonable anatomical constraints. For example, the maximum spatial extent of a pyramidal cell's connection to a feedback inhibitory cell is 1 mm. The probability that the pyramidal cell will connect to any one feedback inhibitory neuron is 0.2. The space constant for the exponential decay in connection strength from the pyramidal cell to the interneuron is 5 mm. As we shall see in later sections, these simple statistical rules are sufficient for generating realistic behavior in the network model. (Specifics on connection parameters for all synaptic pathways can be found in chapter appendix F).

### 12.5.2 Numbers of Neurons

The simplification needed to construct our realistic model involves not only the complexity of the modeled neurons and interneuronal connections but also the number of neurons being simulated. The piriform cortex of the rat contains on the order of  $10^6$  neurons and covers an area that is roughly 10 mm by 6 mm (Haberly 1990). However, the model described here consists of only 4,500 cells, representing three populations of neurons (1,500 each of superficial pyramidal, feedforward inhibitory, and feedback inhibitory neurons). One way of thinking about this simplification is that individual simulated neurons really represent the average responses of a much larger set of neurons in their immediate vicinity. Thus, although single neurons are modeled to have cellular properties like those of real individual cells (see below), we adjust for the neurons missing in the simulation by artificially increasing the strength of synaptic connections between cells. In this sense, a single modeled cell integrates information as a single neuron, but communicates the results as if it represented the average output of multiple neurons.

### 12.5.3 Types of Neurons

Although our network model of piriform cortex comprises three types of neurons, there are many more than three types in the real cortex (Haberly 1983). For example, two different types of pyramidal neurons have been identified, each with somewhat different physiological properties (Tseng and Haberly 1989). Moreover, there is an additional excitatory cell type that is nonpyramidal in structure, the so-called multipolar cell (Tseng and Haberly 1989; Hoffman and Haberly 1989), which also has distinct and interesting physiological properties (although there are far fewer multipolar cells than pyramidal neurons). Again, for the sake of simplicity these cell types were not included in the original model. Later iterations of the network model will likely include members of these other neuron classes.

### 12.5.4 Biophysical Properties

Another level of simplification at the single-cell level involves the membrane properties of the modeled neurons. Although our model includes Hodgkin and Huxley-like currents, many additional types of voltage-gated conductances known to exist in piriform pyramidal neurons (Banks, Haberly, and Jackson 1996; Constanti and Sim 1987a; Constanti et al. 1985, Constanti and Galvan 1983a, 1983b) are not included. Instead, we modeled only those currents associated with the fast sodium and potassium currents responsible for spike generation. To avoid the computationally expensive calculations associated with the Hodgkin-Huxley equation, the modeled currents were further simplified by activating the sodium and potassium currents only when the membrane potential crossed a fixed threshold. At that point, a very fast  $\text{Na}^+$  current would activate, followed by a slower  $\text{K}^+$  current, thus accurately re-creating the currents and membrane potentials associated with real action potentials, but without the computational overhead of a full Hodgkin-Huxley current. A serious shortcoming of this approach, however, is that it eliminates the contribution of voltage-gated currents to subthreshold activity, which recent studies have suggested is important to neural computation (Protopapas and Bower 1998b). Faster computers no longer make these compromises with conductances as necessary.

As with voltage-gated currents, synaptic conductances are modeled neglecting computationally expensive details like the kinetics of ligand binding, neurotransmitter uptake, and so on. Instead, changes in synaptic conductance are modeled as the difference of exponential functions, which approximates the shape of EPSPs seen in experimental studies (see “Synaptic Currents” in chapter appendix B).

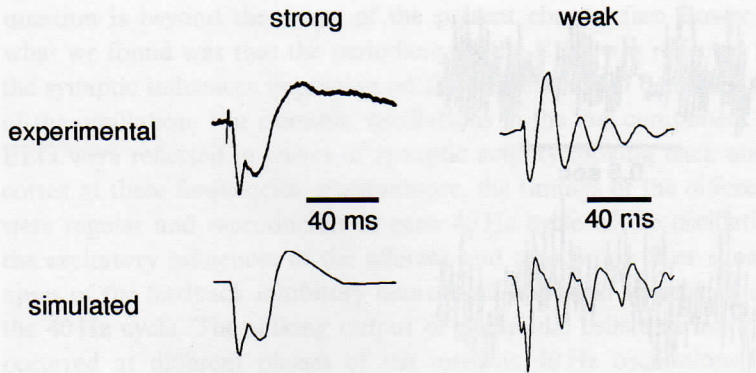
## 12.6 Modeling Results

Our primary modeling objective was to generate the characteristic pattern of the electroencephalogram (EEG; see chapter appendix A for definition) seen in piriform cortex (Freeman and Schneider 1982; Freeman 1960). Because the shape of the EEG is presumably directly related to the interaction of many network components, we thought that it would provide a good measure of the basic validity of the model's structure. In accordance with our approach to modeling, we initially tuned our model on a physiological measure not directly or obviously related to our specific modeling objective, in this case, the surface evoked responses of the network to direct LOT stimulation. At the time, we were not aware of any direct relationship between these responses and the activity patterns seen in the EEG. As will become clear in later sections, the model suggested that there was indeed a direct relationship.

### 12.6.1 Tuning Network Parameters

The response of piriform cortex to LOT stimulation is very well described experimentally as this is one of the ways in which experimentalists have traditionally probed the organization of this structure (Haberly 1973a; Haberly and Bower 1984; Bower and Haberly 1986; Freeman 1968a, 1968b). This makes the evoked potential responses a good measure for model tuning. It has also been demonstrated that small changes in the strength of the LOT shock result in distinctly different spatial and temporal patterns of surface evoked potentials (Freeman 1968b). Specifically, as shown in figure 12.3, a weak shock to the LOT produces a prolonged damped oscillatory response, while a strong shock produces a short-duration biphasic response. From the point of view of modeling, this means that different model results can be compared by changing only a single parameter, in this case, the strength of the stimulus presented to the model's LOT. When tuning any model, it is an advantage to be able to test the results by changing a single stimulus variable. Our model has the added advantage that the stimulus strength dependence of the actual cortex is somewhat unusual because a weak shock generates more sustained activity than a strong shock.

Figure 12.3 demonstrates that the simulation replicates quite well the shock strength dependence of cortical evoked potentials. Furthermore, as described in more detail in Wilson and Bower 1992, the model accounted for the shock strength dependence of the cortex in a way that was not expected prior to the simulation results. For example, the simulations suggested that the reactivation of the rostral part of the cortex at the beginning of the second phase of oscillation of the network

**Figure 12.3**

Comparison of field potential responses of simulated and biological piriform cortex to strong and weak shocks of the LOT. Experimental data for strong shock are taken from Haberly 1973, while experimental data for weak shock results are taken from Freeman 1968. All simulation data come from Wilson and Bower 1992.

was a result of the interaction between the spread of activity throughout the whole network and the time constants of locally activated inhibitory neurons. The role of inhibitory neurons in cortical oscillations has since been proposed by numerous other modelers (Bush and Sejnowski 1996; Jefferys, Traub, and Whittington 1996) and recently demonstrated physiologically for olfactory structures in insects (MacLeod and Laurent 1996). At the time, however, it was unexpected.

#### 12.6.2 Simulating the Electroencephalogram

Once the network was tuned to produce the evoked potential responses characteristic of real piriform cortex, model parameters were fixed and a more natural pattern of afferent input was applied. Because it is known that olfactory bulb field potentials oscillate at similar frequencies to those seen in the olfactory cortex (Bressler 1984; Freeman and Schneider 1982), the model was initially presented with low levels of phasic afferent input. Under these conditions, and without any change in model parameters, the modeled cortex generated an EEG with both the high-frequency (40–60 Hz) and low-frequency (5–12 Hz) components characteristic of the real cortex (see figure 12.4), although it was perhaps not terribly surprising since the input pattern had similar frequencies. What we did not expect was that the cortex produced the same shape EEG even without a temporally patterned input. The fact that this simulation replicates both principal frequency components of the EEG, given either phasic or tonic input, suggested that these oscillatory patterns may be intrinsic

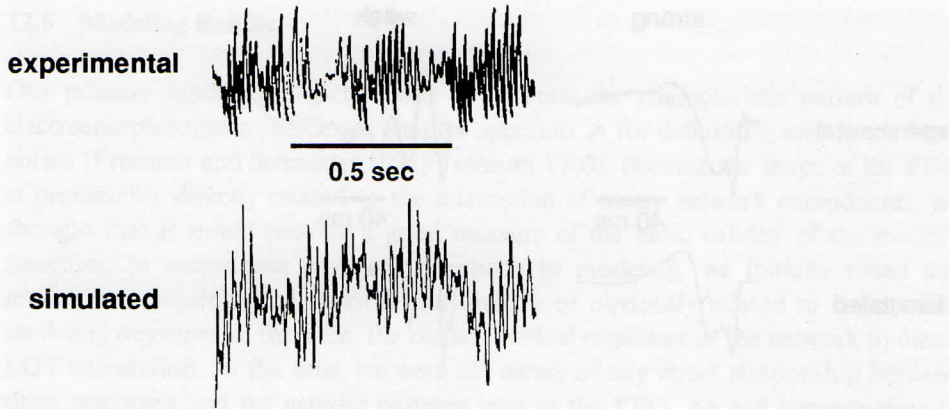


**Figure 12.4**

Comparison of EEG results from physiological experiments and the network model. Fast oscillations constitute the gamma rhythm (40–60 Hz), while the modulation of gamma oscillations represents the theta rhythm (5–12 Hz). Simulation data come from Wilson and Bower 1992 and experimental data from Bressler 1984.

properties of the circuitry itself. Freeman reached the same conclusion from experiments where the LOT was cut and low levels of stimulation given to the cortical side of the cut tract (Freeman 1968a). Thus experimental and simulation results both support the idea that the piriform cortex oscillates intrinsically at frequencies appropriate to the phasic patterns of afferent activity it would naturally receive during the active sniffing cycle of the animal.

#### 12.6.3 Functional Significance

The simulation experiments described here were the first step in our efforts to use modeling techniques to explore how the olfactory cortex might contribute to recognizing odors. Although our intention was to use the simulation of network dynamics to test the validity of the model's basic structure, even at this initial stage, the simulations led to several new and unexpected ideas about the possible significance of the dynamical behavior of piriform cortex.

One of the surprises of this early modeling effort was that the cortex itself seemed to oscillate intrinsically, even when presented with continuous random patterns of input, and even though the cells from which the model was built had no intrinsic oscillatory properties of their own. Thus the oscillations emerged from the structure of the network itself. This observation led us to examine more carefully which aspects of network structure underlie oscillations, although a detailed answer to this

question is beyond the scope of the present chapter (see Bower 1995b). In short, what we found was that the periodicity in the EEG was reflected in a periodicity in the synaptic influences impinging on the pyramidal cell dendrites during each phase of the oscillation. For example, oscillations in the fast component (40–60 Hz) of the EEG were reflected in waves of synaptic activity moving back and forth across the cortex at these frequencies. Furthermore, the timings of the different synaptic inputs were regular and reproducible in each 40 Hz cycle of the oscillation. For example, the excitatory influences of the afferent and association fiber synapses and the synapses of the feedback inhibitory neurons all appeared to peak at different phases of the 40 Hz cycle. The spiking output of pyramidal cells and inhibitory neurons also occurred at different phases of the intrinsic 40 Hz oscillations. Given that theta bursts are correlated with the sniffing rate of the animal (Bressler 1984; Freeman and Schneider 1982), this suggested that the theta oscillations reflect an iterative computational process leading to odor recognition (Bower 1995b).

Whatever the computational significance of the oscillations, the most immediate implication of these results was that the oscillations arise indirectly from network-based mechanisms that control the timing of information arriving on the dendrites of cortical pyramidal cells (Bower 1990). In this view, the oscillations themselves are an epiphenomenon, reflecting more complex mechanisms that serve to control the timing of synaptic influences throughout the network. This in turn suggested that pyramidal cells might require that synaptic inputs of different sorts arrive at particular times with respect to each other, a conclusion also implied in current-source-density studies by Ketchum and Haberly (1993b). Pyramidal cells might therefore work something like internal combustion engines in which the cylinders need to be sparked in the right time and in the right sequence for proper functioning. Exploring this question, however, required the development of a much more realistic model of single pyramidal cell dendrites.

## 12.7 Detailed Model of a Single Pyramidal Cell

### 12.7.1 Structure of the Pyramidal Cell Model

To explore the sensitivity of pyramidal cell responses to different patterns of synaptic input, we needed to construct a model cell with realistic dendritic morphology and the proper passive and active membrane properties. Because several other chapters (3, 4, and 5) in this book deal with constructing single-cell models, we shall only summarize the approach taken here (additional details can be found in Protopapas and Bower 1998a, 1998b).

### 12.7.2 Passive Properties

As is often the case with realistic single-cell models, the morphology of the model was taken from the anatomical reconstruction of a real neuron (anatomy performed by Mark Domroese of the University of Wisconsin). The next step was to establish the passive properties of the model, using experimentally obtained values for input resistance,  $R_{in}$ , the membrane time constant,  $\tau_0$ , and the first equalizing time constant,  $\tau_1$ , from traces of membrane potential in response to constant current injection. Experimental values for these passive properties were obtained in our laboratory from whole-cell recordings in piriform cortex slices bathed in Cs<sup>+</sup> (non-specific K<sup>+</sup> channel blocker) and TTX (Na<sup>+</sup> channel blocker). Using experimental values for  $R_{in}$ ,  $\tau_0$ , and  $\tau_1$  and standard methods, we were able to calculate values for the model parameters  $R_m$  (specific transmembrane resistance),  $R_a$  (specific axial resistance), and  $C_m$  (specific membrane capacitance; Protopapas and Bower 1998b; Rapp, Segev, and Yarom 1994; Major et al. 1994). See table 12.1 for parameter values.

**Table 12.1**  
Parameter values for full and reduced models of piriform cortex pyramidal cell

	Full model	Reduced model
Number of compartments	1,089	15
Voltage-gated conductances		
Fast Na <sup>+</sup>	Fast Na <sup>+</sup>	Fast Na <sup>+</sup>
Persistent Na <sup>+</sup>	Persistent Na <sup>+</sup>	Persistent Na <sup>+</sup>
Delayed-rectifier K <sup>+</sup>	Delayed-rectifier K <sup>+</sup>	Delayed-rectifier K <sup>+</sup>
M-current K <sup>+</sup>	M-current K <sup>+</sup>	M-current K <sup>+</sup>
Slow AHP K <sup>+</sup>	Slow AHP K <sup>+</sup>	Slow AHP K <sup>+</sup>
A K <sup>+</sup>	A K <sup>+</sup>	A K <sup>+</sup>
Slow Ca <sup>2+</sup>	Slow Ca <sup>2+</sup>	Slow Ca <sup>2+</sup>
Fast Ca <sup>2+</sup>	Fast Ca <sup>2+</sup>	Fast Ca <sup>2+</sup>
Synaptic conductances		
Non-NMDA	Non-NMDA	Non-NMDA
NMDA	NMDA	NMDA
GABA <sub>A</sub>	GABA <sub>A</sub>	GABA <sub>A</sub>
GABA <sub>B</sub>	GABA <sub>B</sub>	GABA <sub>B</sub>
Average electrotonic length of compartment ( $\lambda$ )	0.0184	0.0916
$R_{IN}$ (MΩ)	47.6	58.1
$R_m$ (kΩ · cm <sup>2</sup> )	30.0	5.0
$R_a$ (kΩ · cm)	0.350	58
$C_m$ (μF/cm <sup>2</sup> )	0.80	4.36
$\tau_0$ (msec)	23.6	22.0
$\tau_1$ (msec)	2.10	2.15

### 12.7.3 Active Conductances

Any model of realistic single-cell behavior must include active membrane properties. In the case of piriform cortex pyramidal cells, a number of voltage-gated currents have been characterized in the pyramidal cell, including at least one  $\text{Ca}^{2+}$  current (Constanti et al. 1985) and several potassium currents: a fast inward rectifier (Constanti and Galvan 1983a), a noninactivating muscarinic (M) current (Constanti and Galvan 1983b; Constanti and Sim 1987a), a slow  $\text{Ca}^{2+}$ -activated afterhyperpolarization (AHP) current (Constanti and Sim 1987a), and an A-current (Banks, Haberly, and Jackson 1996). Because piriform pyramidal neurons are known to have fast spikes, we assume the presence of fast sodium and delayed-rectifier potassium currents. Furthermore, we found that the addition of a persistent sodium current greatly improved the behavior of the model. Although there is no direct evidence that this current exists in the piriform pyramidal cell, it has been shown to exist in pyramidal neurons from the hippocampus (French et al. 1990). When voltage clamp data were available for piriform currents, we used these in our model; otherwise, we borrowed hippocampal voltage clamp data from previously modeled currents (Traub et al. 1991; McCormick and Huguenard 1992). The internal calcium dynamics used to activate the AHP current were a simplified model of the one used by Sala and Hernandez-Cruz (1990; see also chapter 6, this volume).

### 12.7.4 Synaptic Conductances

To examine the effect of patterns of synaptic inputs on the dendrites of the pyramidal cell, we needed to add realistic distributions of synaptic conductances to the modeled dendrite. As shown in figure 12.2, the synaptic input to piriform pyramidal cells is organized in a laminar fashion. Afferent projections from the olfactory bulb arrive via the LOT and terminate on the most distal part of the apical dendrite (Heimer 1968; Rodriguez and Haberly 1989; Ketchum and Haberly 1993a; Price 1973; Haberly and Behan 1983), while excitatory projections originating within the cortex terminate on more proximal regions of the dendrite (Bower and Haberly 1986; Haberly and Bower 1984).

We also had to provide the synapses themselves with realistic kinetic properties. Pharmacological experiments performed in rat piriform cortex slices show that LOT-induced excitation of pyramidal neurons is mediated by both NMDA and non-NMDA receptors in layer Ia (Kanter and Haberly 1990; Jung, Larson, and Lynch 1990). A slow-acting  $\text{GABA}_B \text{K}^+$ -mediated inhibition present in layer Ia is believed to originate in feedforward inhibitory neurons also excited by LOT afferents (Tseng and Haberly 1988). In the model, afferent excitation (with NMDA and non-NMDA

components) and  $\text{GABA}_B$  inhibition are restricted to layer Ia. The layer-Ib portion of the dendrite has also been shown to contain both NMDA and non-NMDA type receptors (Kanter and Haberly 1990) and, as in the network model,  $\text{GABA}_A$ -type receptors are present in the layer-II portion of the dendrite and also the soma (Tseng and Haberly 1988).

The time constants for the non-NMDA synapses were chosen to fit experimental data on the time course of non-NMDA conductances in hippocampal pyramidal cells (Mason, Nicoll, and Stratford 1991). Our model of NMDA-mediated synapses was identical to that used by Holmes and Levy (1990; see also chapter 6, this volume). Time constants for  $\text{GABA}_B$  synapses were chosen to match experimental data on the time course of  $\text{GABA}_B$  responses in rat hippocampal neurons (Ling and Benardo 1994). Time constants for  $\text{GABA}_A$  responses were taken from Pearce 1993. In the model, the parameters for NMDA and non-NMDA synapses in layer Ib were identical to those used in layer Ia, except that channel densities were varied. Specifically, to account for the stronger NMDA response in layer Ib seen experimentally (Kanter and Haberly 1990), the channel density of the NMDA receptors was made twice as large in layer Ib.

#### 12.7.5 Simplifying Cellular Components

To conform to computational constraints, and because of a lack of experimental data, a number of simplifications to the single-cell model had to be made. Dendritic spines were not modeled explicitly, but rather were included as an increase in dendritic membrane area. Similarly, second-messenger pathways for metabotropic synaptic receptors and complex calcium dynamics (e.g.,  $\text{Ca}^{2+}$  release from intracellular stores) were not included in the model, even though they are known to exist (Tseng and Haberly 1988; Sah 1996). These omissions were permitted primarily in the name of computational efficiency. Fortunately, the model still exhibits reasonable approximations to real behavior (see below).

A further simplification was the absence of voltage-gated channels in the dendritic tree. Although numerous recent reports have shown the existence of voltage-gated channels in the dendritic trees of neocortical and hippocampal pyramidal cells (Stuart and Sakmann 1994; Magee and Johnston 1995), adequate data do not yet exist for the neuron we are modeling, and there is evidence to suggest that some voltage-gated channels that exist in the dendrites of neocortical and hippocampal pyramidal neurons may not exist in the dendrites of piriform pyramidal cells (Westenbroek et al. 1992). Furthermore, evidence in hippocampal pyramidal neurons suggests that active dendritic properties may primarily serve a role in synaptic plasticity and additionally may only come into play when a somatic spike has

already been elicited (Magee and Johnston 1997; Markram et al. 1997). Because the present single-cell model does not address issues of plasticity, we felt that we could neglect the active properties of the dendrite. Future iterations of the single-cell and network models will almost certainly have to include active dendritic conductances.

#### 12.7.6 Tuning Neuronal Parameters

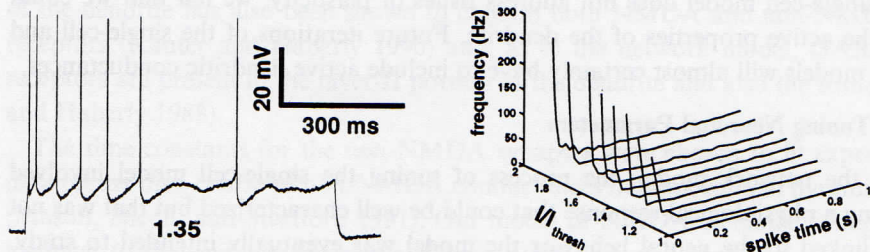
As with the network model, the process of tuning the single-cell model involved identifying a physiological response that could be well characterized but that was not directly linked to the neural behavior the model was eventually intended to study. The measure chosen was *in vitro* responses to somatic current injection (Protopapas and Bower 1998b; Barkai and Hasselmo 1994). Because this nonphysiological stimulus generates characteristic cellular responses, intracellular current injection is comparable to the electrical LOT shock used to tune the network model.

In most realistic single-cell models, the most poorly constrained parameters are the densities of the active channels. In the present case, this set of important parameters was tuned by matching the spiking behavior of the model to experimental *F/I* (frequency against current injection) plots obtained with different levels of somatic current injection (Barkai and Hasselmo 1994). In addition, the ability of the model to match subthreshold events and the actual spike shapes seen in experimental traces were also quantified. When simulated and experimental spiking behavior are compared (figure 12.5), much of the behavior seen in the real spike train can also be seen in the model spike train, for example, the two fast spikes at the beginning of the train and the subthreshold oscillations following the last spike.

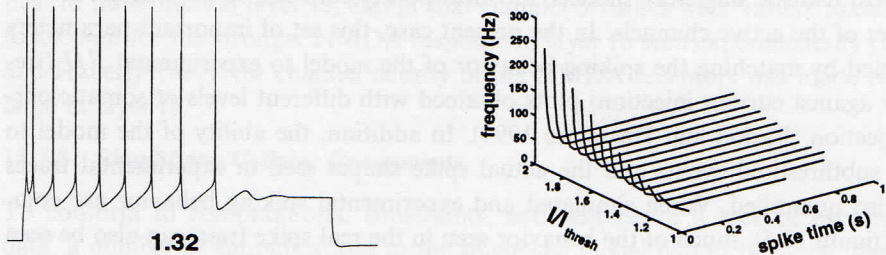
#### 12.7.7 Response to Synaptic Input

Once the model was tuned, synaptic input was applied to the dendrite of the cell and the responses measured. Because we were interested in exploring how synaptic activity patterns suggested by the network model and experimental studies (Ketchum and Haberly 1993a, 1993b, 1993c) might influence the information-processing properties of this neuron, we applied a synaptic input pattern believed to underlie the 40 Hz oscillations seen in the EEG (Ketchum and Haberly 1993b, 1993c), and then examined the effect of this pattern on the intracellular response of the pyramidal cell. Figure 12.6A shows how a change in the synaptic input underlying a single 40 Hz oscillation can affect subsequent oscillations during the course of a theta (5–12 Hz) oscillation. This suggests that the activity induced during the course of a single 40 Hz oscillation is not independent of the activity underlying nearby oscillations. Therefore, the computations that the neuron performs during the course of a single theta

## EXPERIMENT



## FULL MODEL



## REDUCED MODEL

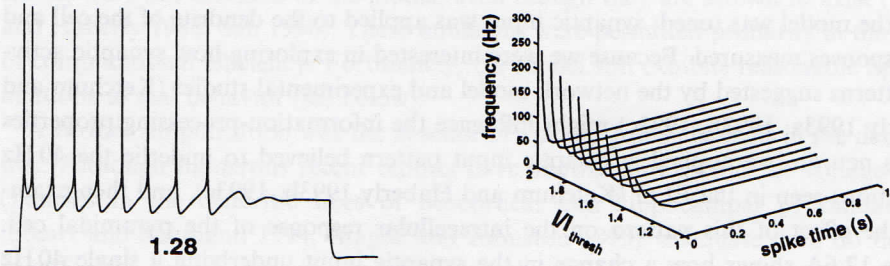


**Figure 12.5**

Comparison of full and reduced models to experimental response to current injection. The numbers below the voltage traces indicate the threshold normalized current injection used in each case.  $I_{\text{threshold}} = 1$ .

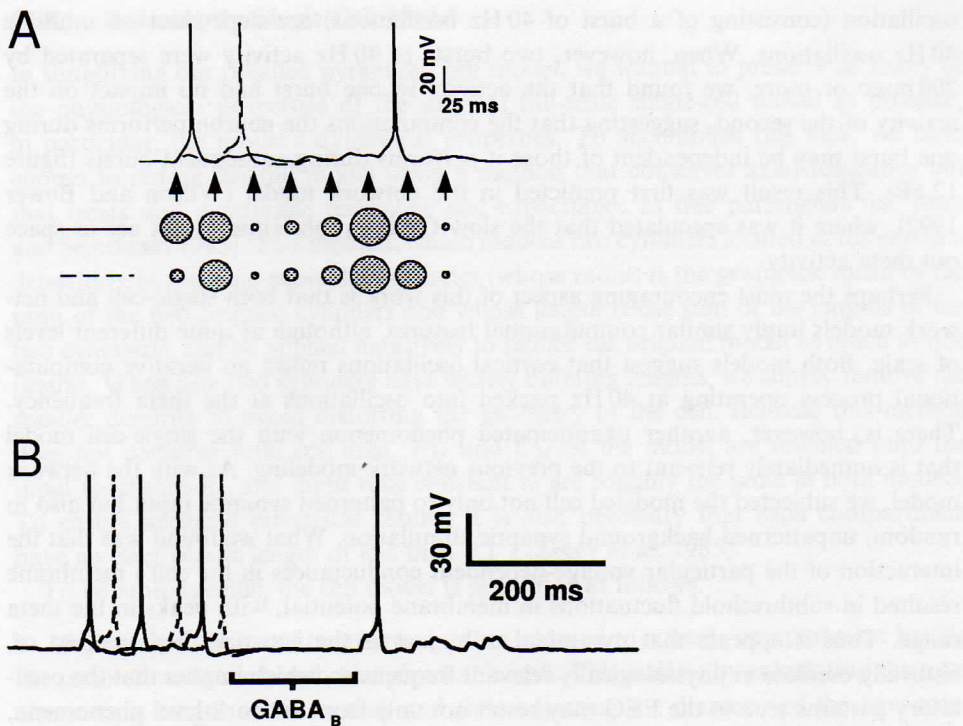


**Figure 12.6**  
 Effects of the input underlying a single 40 Hz oscillation during subsequent 40 Hz oscillations. Two intracellular traces from the detailed single-cell model are shown. The input underlying each trace is identical except that the input for the first 40 Hz oscillation is much smaller for the dotted trace than for the solid. The divergence between the two traces lasts approximately 90 msec showing that the effects of the input underlying a single 40 Hz oscillation can last much longer than the 25 msec duration of single oscillation. (B) Two bursts of 40 Hz activity (believed to represent activity underlying single theta oscillations) are separated by 200 msec. Again, the figure shows two overlapping traces; in this case, the input underlying the two traces is identical except in the first burst of 40 Hz activity. As can be seen, despite the difference in the initial burst, the second set of bursts is identical, suggesting that activity in the previous burst has little impact on subsequent bursts provided they are separated by 200 msec. Such a separation in time can be accounted for biologically by the presence of a slow GABA<sub>B</sub> inhibition.

oscillation (consisting of a burst of 40 Hz oscillations) are dependent on multiple 40 Hz oscillations. When, however, two bursts of 40 Hz activity were separated by 200 msec or more, we found that the activity in one burst had no impact on the activity of the second, suggesting that the computations the neuron performs during one burst may be independent of those it performs during subsequent bursts (figure 12.6B). This result was first predicted in the network model (Wilson and Bower 1992), where it was speculated that the slow GABA<sub>B</sub> inhibition might act to space out theta activity.

Perhaps the most encouraging aspect of this work is that both single-cell and network models imply similar computational features, although at quite different levels of scale. Both models suggest that cortical oscillations reflect an iterative computational process operating at 40 Hz packed into oscillations at the theta frequency. There is, however, another unanticipated phenomenon with the single-cell model that is immediately relevant to the previous network modeling. As with the network model, we subjected the modeled cell not only to patterned synaptic input but also to random, unpattered background synaptic stimulation. What we found was that the interaction of the particular voltage-dependent conductances in the cell's membrane resulted in subthreshold fluctuations in membrane potential, with peaks in the theta range. Thus it appears that pyramidal cells, just as the network they are part of, naturally oscillate at physiologically relevant frequencies, which implies that the oscillatory patterns seen in the EEG may result not only from network-level phenomena, but also from the emergent properties of the voltage-dependent conductances. Thus, there also appears to be a resonance between network and single cell properties.

To study this relationship further, and to pursue our computational interpretation of cortical oscillations, we had reconstitute a network-level simulation based on neurons with more realistic biophysical properties. Accordingly, just as our original network models led us to single-cell modeling, now our single-cell modeling has led us back to network simulations.

### 12.8 Refining the Network Model

The specific objective of our third stage of modeling of olfactory cortex is to construct a network model based on more sophisticated pyramidal cell simulations. While computers are dramatically more powerful now than they were when we built our first network model twelve years ago (on an IBM XT!), they are still not powerful enough to construct a large-scale network model out of full-scale single-cell simulations. It is therefore necessary to reduce the complexity of the single-cell models.

### 12.8.1 Reducing the Single-Cell Model

In simplifying our detailed pyramidal cell model, we wanted to preserve as many of the physiological properties of the original full-scale single-cell model as possible, in particular, the model's dynamical properties. To accomplish this task, we have chosen to reduce the full model using a method that conserves axial resistance but that treats unit membrane resistance and capacitance as free parameters (cf. Bush and Sejnowski 1993). This method, which reduces two cylinders located at the end of a dendritic tree into one equivalent cylinder (whose radius is the geometric mean of the radii of the two original cylinders and whose length is the sum of the lengths of the two cylinders), can be applied iteratively to reduce the original model as much as one desires. When any two cylinders have widely differing lengths, we simply remove the smaller dendrite to avoid distorting the geometry of the cell. Because this method does not conserve total cell area,  $R_M$  and  $C_M$  of the model are rescaled until the input resistance  $R_{in}$  and input time constant  $\tau_0$  are roughly the same in both models. To ensure accurate numerical results, it is also necessary that each compartment have an electrotonic length of less than  $0.1 \lambda$  (Segev et al. 1985).

To be more specific, the cell model is simplified as follows:

1. Unbranched chains of compartments are reduced to a single compartment having the same electrotonic length and physical length. This is done by calculating the total electrotonic length of the branch and then adjusting the diameter of the new compartment to give the same total electrotonic length.
2. Branches are collapsed into single compartments, starting from the distal end and proceeding inward, according to the Bush and Sejnowski (1993) algorithm described above. This is repeated until only five compartments remain: a basal dendritic compartment, the soma compartment, and an apical dendrite in three compartments (proximal layer 1b, distal layer 1b, and layer 1a). The apical dendrite compartments, which can be joined together, are kept separate because the connection topology of the model requires separate compartments. At this point, we have five compartments.
3. Because the basal and apical dendritic compartments are considerably longer than the  $0.1 \lambda$  limit normally considered to be the maximum length compatible with numerical accuracy, we subdivide each of the dendritic compartments into two to six compartments, which results in fifteen compartments all less than  $0.1 \lambda$  in length. One thing to note is that this method assumes a passive dendritic tree and is therefore not likely to be valid with active dendrites. In the current version of our model, however, all the active conductances are located in the soma.

The fact that the full and reduced models both contain the same voltage-gated channel types in roughly equal proportions implies that they will have very similar active properties. As with all our models, however, we first test the reduced model's performance with a functionally neutral response pattern, in this case, the same measure we applied to the full single-cell model: the response of the cell to somatic current injections. In figure 12.5, we have plotted the spike frequency against current injection during a series of increasing current steps for the two models. The results demonstrate almost identical performances, which is not surprising given that the reduced model was tuned to have an input resistance, as well as membrane and equalizing time constants  $\tau_0$  and  $\tau_1$ , similar to those of the full model. Table 12.1 compares the behavior and parameters of the two models for several additional measures. The only significant differences are seen in the number of compartments, the specific transmembrane resistance,  $R_m$ , the specific axial resistance,  $R_a$ , the specific membrane capacitance,  $C_m$ , and, most important, the execution time (2.22 min for the full model vs. 3 sec for the reduced model for simulation of 100 msec on a 200 MHz PC running Linux). The astute reader may additionally note that the average electrotonic length of compartments in the full and reduced models suggests that total electrotonic length is not conserved between the full and reduced models. This may be unavoidable because many individual dendrites are collapsed into single dendrites during the reduction process.

### 12.8.2 The Costs of Model Simplification

Given that the transient responses of the complex and simplified models are essentially the same, it is likely that under many conditions both models will respond almost identically to individual synaptic inputs. Because the geometrical complexity of the neuron has been dramatically decreased, however, some patterns of single-cell response will no longer be possible. For example, in the reduced model multiple dendritic branches are represented by single compartments or strings of compartments. Because a small high-resistance compartment in the detailed model will be represented by a lower-resistance compartment in the reduced model, synaptic inputs will see different input resistances in the different models. Perhaps more important, it will not be possible with the reduced model to study how particular spatial patterns of synaptic inputs on individual dendrites might functionally affect cellular or network output. This means, for example, that in the network model we will not be able to study the consequences of synaptic segregation on individual dendritic branches. Furthermore, even though particular spatial patterns of synaptic input on single branches are important, as has been suggested (Koch, Poggio and Torre 1982), they

will not figure in our network simulations. Because these questions can be studied using our existing single-cell simulation, our research will almost certainly continue to be based on the iterative use of the single-cell and network models.

### 12.9 Discussion

One of the most basic assumptions underlying the construction of realistic simulations is that the structure of the nervous system, if we respect it, will lead us to ideas about its function. In this chapter, we have attempted to illustrate how our simulations of olfactory cortex have led us to new and unanticipated functional ideas as well as to new simulations at different levels of scale with which to test them. This is the power and excitement of realistic modeling. For several fortuitous reasons, our work in the olfactory system has also allowed us to demonstrate the process of extracting functional ideas from neural structure without the problem of imposing ad hoc theoretical interpretations on neural data.

At the time our simulations were first completed (Wilson and Bower 1987), there was little interest outside of the olfactory community in cerebral cortical oscillations. Indeed, a paper submitted to *Science* in 1988 describing the implications of our network simulations for the origins of cortical oscillations was rejected without review as being "not interesting to a broad audience." In 1989 however, *Science* published a report describing oscillations of similar frequencies in visual cortex (Gray et al. 1989). Since that time, there has been tremendous interest in cortical oscillations involving the visual system.

The primary reason for this interest was that changes in the oscillatory structure of the response seemed to be directly related to changes in the visual stimulus presented. While, by itself, this was probably not too exciting, several years earlier it had been proposed on theoretical grounds that synchronous neuronal firing might provide the means of solving what is known in the machine vision and artificial intelligence fields as "the binding problem," the presumed difficulty that feature detection-based systems have in assigning multiple attributes (e.g., color, texture, etc.) to the same object. It was proposed that by synchronized neuronal firing, multiple attributes could be represented together (von der Malsburg and Schneider 1986) and Gray et al. (1989) had found synchronous oscillations in visual cortex that seemed to be related to the nature of the stimulus.

What has happened since that 1989 report was published is nothing short of remarkable. Large numbers of meetings have been held and models generated to look at the mechanisms and functional significance of cortical oscillations. Not only have

oscillations been linked to the binding problem, but other authors have extended their applicability to models of visual attention (Niebur, Koch, and Rosin 1993) and even consciousness (Crick and Koch 1990). These ideas continue to have a substantial influence on both experimental (Whittington, Traub, and Jefferys 1995) and theoretical (Traub et al. 1996) neurobiology. Most of the models used to investigate these phenomena, however, have been "demonstration models," intended, with greater or fewer real "neural features," to support the plausibility of a particular functional idea.

Our own interpretation of the significance of oscillations in olfactory cortex is very different from the interpretation applied to the visual system. That the model we used to investigate oscillations was firmly based on real biology led us to suspect the interpretation of the oscillations applied to the visual system for several practical reasons (Wilson and Bower 1991). First, as in our models of olfactory cortex, the oscillations recorded in the visual system were of the EEG/evoked potential type. Unfortunately, most theorists assumed that the timing of evoked potentials and EEGs directly reflected the timing of pyramidal cell spiking. From our models, we knew that these field potential effects were actually related to synaptic inputs on dendrites, and not necessarily to spike outputs. Accordingly, the actual patterns of spikes could not be directly inferred from the EEG or evoked potential patterns. Second, from our simulations of a more visual cortex-like structure (based on the olfactory cortex simulation; Wilson and Bower 1991), we predicted that the oscillations would not be instantaneous, continuous, or even very regular, as was implied by simple versions of the binding/attention hypothesis. Finally, it seemed quite unlikely to us, given the duration of the effects of the synaptic input underlying a single 40 Hz oscillation, that these neurons would do a good job of detecting millisecond coincidences in firing (Protopapas and Bower 1998a).

For each of these reasons, we are skeptical about a direct role for oscillations in neural coding. Instead, as we suggested many years ago, based on our realistic network models (Wilson and Bower 1991), cortical oscillations are more likely to indirectly reflect network and single-cell processes involved in regulating the timing of synaptic activity in and between networks. Recent experiments demonstrating that different structures within the somatosensory system start to oscillate synchronously prior to the onset of sensory or motor behavior (Nicolelis et al. 1995) are consistent with the idea that the oscillations reflect the control of synaptic timing and the flow of information. Furthermore, we have suspected for many years that oscillatory activity patterns also indirectly reflect the timing and organization of computational cycles within cortical circuits. Finally, whatever the functional role of oscillations in

cortical networks, we believe it is more useful to develop theories based on realistic models than to try to squeeze brain circuits into ad hoc theories, where once the model has demonstrated plausibility, the modeling is done. As demonstrated in this chapter, realistic modeling is never done. There are always more interesting relationships to discover.

### Acknowledgments

We wish to thank Fidel Santamaria and Jenny Forss for their helpful comments on the text; Mark Domroese for providing us with an anatomically stained pyramidal cell for our single-cell modeling work; and John Miller and Gwen Jacobs for their generous help in digitizing the cell's anatomy. Chris Assad was also very helpful in generating the contour plots that are basis for figure 12.7. Finally, we wish to thank Matt Wilson, who wrote the network modeling chapter in the first edition of this volume, on which this chapter is based.

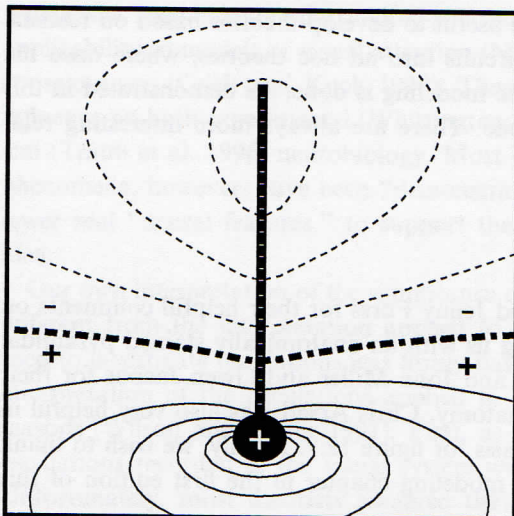
### Appendix A: Using the Model to Generate Field Potential Events

This appendix describes how evoked potential and EEG responses were derived from model activity. While both kinds of responses fall under the category of field potential recording, what differentiates them is the experimental context in which the field potentials are recorded. *Evoked potential* refers to a change in the extracellularly recorded field potential in response to a specific stimulus (e.g., a shock to the LOT). By contrast, *EEG*, a more general term, refers to field potential recordings taken at the cortical surface or even the scalp, often in the absence of a well-characterized stimulus and almost always over a large area of the brain. For example, EEG recordings are often made while an animal is freely exploring its surroundings, rather than in response to a well-timed shock. The neuronal origin of field potentials is not easy to elucidate, and efforts to do so are still an active area of research (Ketchum and Haberly 1993a, 1993b, 1993c). As we shall see shortly, this difficulty arises from the physics underlying field potentials.

To simulate field potentials in the model, we first calculated the extracellular currents expected to flow through the cortex due to neuronal activity. Neurons, like any electrical entity, must obey Kirchoff's current law, which states that the sum of all currents entering and leaving a circuit node must equal zero. In the case of a neuron, this means that if synaptic current, for example, enters the cell at one point, it must leak from another, thereby generating an extracellular current (see figure 12.7). Because compartmental modeling deals with lumped representations of neurons (i.e., electrical compartments are discrete), field potentials can be calculated using the following equation:

$$\Phi(\vec{d}, t) = \frac{1}{4\pi\sigma} \sum_{i=1}^n \frac{I_i(t)}{d_i}, \quad (12.1)$$

where  $\Phi$  is the field potential in volts,  $I_i$  (equivalent to the transmembrane current in a single compartment) is the total current (in amperes) from the  $i$ th current source into brain tissue of conductivity  $\sigma$  (in Ohms $^{-1}$ meters $^{-1}$ ), and  $d_i$  (in meters) is the distance of the  $i$ th current source from the recording site (Nunez 1981). Note that this equation assumes the extracellular medium is a noncapacitative homogeneous conductor, which is only an approximation to biological reality (Ketchum and Haberly 1993b).

**Figure 12.7**

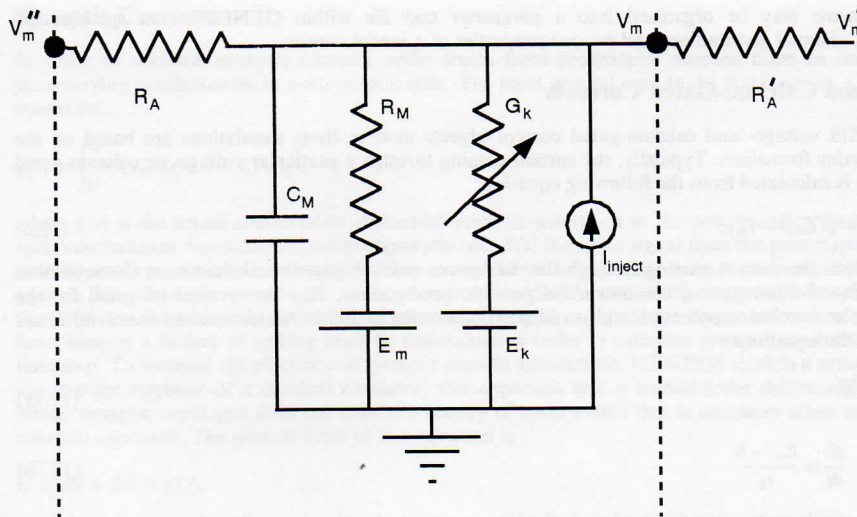
A model cell is shown as it is receiving synchronous excitatory synaptic input along its dendrite. The opening of synaptic channels generates current sinks along the dendrite, while a current source is generated at the soma where current is leaking out of the cell. The current sinks (minus signs) generate negative field potentials shown by the thin dotted isopotential contour lines. Conversely, the current source at the soma is responsible for generating the positive field potentials indicated by the thin solid lines. The thick dotted line represents the region where the field potential has a value of zero. For a more detailed study of field potentials generated by single neurons, specifically during the course of an action potential, see Rall 1962. The figure shown here was inspired by that work.

A brief examination of eq. 12.1 indicates why it is difficult to ascertain which types of physiological activity underlie real field potentials. Specifically, the equation tells us that the size of the field potential increases in amplitude with the magnitude of transmembrane current and decreases with distance between the current source and electrode. Therefore, although neither the position of the electrode nor the magnitude of a transmembrane current can uniquely explain the magnitude of a field potential signal, anatomical constraints such as those imposed by the network model can reduce the number of physiologically plausible explanations for different field potential patterns. Indeed, this was one of the primary motivations in performing the original network modeling study.

In the model, both evoked potentials and the EEG were calculated at positions corresponding to those where physiological measurements had previously been made by other researchers. In the case of the evoked potentials, calculations were made at single surface locations at varying depths. By contrast, the field potentials calculated from forty evenly spaced recording sites on the surface of the simulated cortex were averaged to produce an estimate of the EEG in response to patterned and unpattered input.

#### **Appendix B: Neuronal Objects in GENESIS**

This appendix briefly discusses the mathematical representation of a number of common neuronal objects in GENESIS. (For a more complete description, see Bower and Beeman 1995.)

**Figure 12.8**

Circuit representation of a GENESIS compartment.  $V_m''$ ,  $V_m$ , and  $V_m'$  are the membrane potentials for the left, center, and right compartments demarcated by the dotted lines.  $R_A$  and  $R'_A$  are the axial resistances for the center and right compartments, respectively.  $C_M$ ,  $R_M$ , and  $E_m$  are the membrane capacitance, membrane resistance, and leak current reversal potential, respectively.  $G_k$  is a variable conductance representing synaptic or voltage-gated conductances, and  $E_k$  is the reversal potential associated with the particular conductance.  $I_{inject}$  represents current being injected into the compartment (e.g., current injection through an intracellular electrode).

### Compartmental Representation

Figure 12.8 shows a circuit diagram of a typical GENESIS compartment (chapters 3, 4, and 5, this volume, describe the theoretical basis for compartmental modeling). Values for membrane resistance,  $R_M$ , capacitance,  $C_M$ , and axial resistance,  $R_A$ , are automatically calculated for the compartment object by the “readcell” command. Users set values for specific membrane resistance ( $R_m$ , in  $\Omega \cdot m^2$ ), specific membrane capacitance ( $C_m$ , in Farads per square meter), and specific axial resistance ( $R_a$ , in Ohms times meter). Values for  $R_M$ ,  $C_M$ , and  $R_A$  are calculated using the following relations:

$$C_M = \pi dl C_m \quad (12.2)$$

$$R_M = \frac{R_m}{\pi dl} \quad (12.3)$$

$$R_A = \frac{4lR_a}{\pi d^2}, \quad (12.4)$$

where  $d$  is the diameter and  $l$  is the length of the morphological compartment.

The membrane potential of a compartment is calculated from the following differential equation:

$$C_M \frac{dV_m}{dt} = \frac{(E_m - V_m)}{R_M} + \sum_k [G_k(E_k - V_m)] + \frac{(V_m' - V_m)}{R'_A} + \frac{(V_m'' - V_m)}{R_A} + I_{inject}, \quad (12.5)$$

where all variables are defined in figure 12.8.

Compartments may be organized into a parameter text file within GENESIS that specifies the morphology, channel distribution, and passive properties of a model neuron.

### Voltage- and Calcium-Gated Currents

The GENESIS voltage- and calcium-gated current objects used in these simulations are based on the Hodgkin-Huxley formalism. Typically, the current coming through a particular voltage- or calcium-gated conductance is calculated from the following equation:

$$I(V, t) = m^p h^q \bar{g}(E_{rev} - V_m), \quad (12.6)$$

where  $I(V, t)$  is the current passing through the voltage- or calcium-gated conductance,  $m$  the activation gate,  $h$  the inactivation gate,  $\bar{g}$  the maximum possible conductance,  $E_{rev}$  the reversal potential for the channel,  $V_m$  the membrane potential, and  $p$  and  $q$  exponents for  $m$  and  $h$ . Activation and inactivation are governed by the equations:

$$\frac{dm}{dt} = \frac{m_\infty - m}{\tau_m} \quad (12.7a)$$

$$\text{idem for } h, \quad \frac{dh}{dt} = \frac{h_\infty - h}{\tau_h} \quad (12.7b)$$

where  $m_\infty$  is steady-state activation and  $\tau_m$  is the time constant of activation and both  $m_\infty$  and  $\tau_m$  depend on voltage. Users may define  $m_\infty$  and  $\tau_m$  explicitly or by defining the voltage-dependent rate constants  $\alpha$  and  $\beta$ , which take the following form:

$$\alpha = \frac{A_\alpha + B_\alpha V_m}{C_\alpha + \exp\left(\frac{V_m + D_\alpha}{F}\right)} \quad (12.8a)$$

$$\beta = \frac{A_\beta + B_\beta V_m}{C_\beta + \exp\left(\frac{V_m + D_\beta}{F_\beta}\right)}, \quad (12.8b)$$

where  $A, B, C, D$ , and  $F$  are user-defined parameters. In this case,  $\alpha$  and  $\beta$  may be related to  $m_\infty$  and  $\tau_m$  in the following way:

$$m_\infty = \frac{\alpha_m}{\alpha_m + \beta_m} \quad (12.9a)$$

$$h_\infty = \frac{\alpha_h}{\alpha_h + \beta_h} \quad (12.9b)$$

$$\tau_m = \frac{1}{\alpha_m + \beta_m} \quad (12.10a)$$

$$\tau_h = \frac{1}{\alpha_h + \beta_h}. \quad (12.10b)$$

Calcium-activated currents are modeled in an identical fashion except that rate constants and activation parameters are calcium-dependent instead of voltage-dependent. Using this formalism, one may also combine voltage and calcium activation to create a current that is dependent on both.

Typically, the simulation of Hodgkin and Huxley-type currents is computationally expensive because exponential functions must be calculated at each time step. GENESIS avoids this problem by giving the user the opportunity to create lookup tables that contain precalculated values of rate parameters. Values for rate parameters are evaluated by interpolating from entries contained in the lookup table. This method greatly increases the speed of simulations.

## Synaptic Currents

In order to simulate synaptic currents, spike trains from presynaptic neurons must be converted into time-varying conductances in postsynaptic cells. The most general way to do this is to use a convolution operation:

$$\hat{g}(t) = \int_0^{t_d} G(\lambda)S(t - \lambda - t_l) d\lambda, \quad (12.11)$$

where  $\hat{g}(t)$  is the actual conductance elicited by synaptic activation in the postsynaptic cell,  $G(t)$  the synaptic conductance waveform for the postsynaptic cell,  $S(t)$  the spike signal from the presynaptic cell,  $t_d$  the time interval over which incoming spikes are convolved with the conductance waveform, and  $t_l$  the propagation delay from the presynaptic to the postsynaptic cell. The convolution approach has the advantage that  $G(t)$  can be arbitrarily defined. Unfortunately, it requires significant computational or storage overhead because a history of spiking must be maintained in order to calculate synaptic conductance at every time step. To increase the efficiency of synaptic current simulations, GENESIS models a synaptic input as the impulse response of a damped oscillator; this approach uses a second-order differential equation to model synaptic input and does not require a history of spike events that is necessary when using the convolution approach. The general form of this equation is

$$\ddot{G} + \alpha \dot{G} + \beta G = x(t), \quad (12.12)$$

with

$$\alpha = \frac{\tau_1 + \tau_2}{\tau_1 \tau_2}, \quad \beta = \frac{1}{\tau_1 \tau_2}. \quad (12.13)$$

The impulse response of this system ( $x(t) = \delta(t)$ ) with initial conditions of  $G(0)$  has the following dual exponential form:

$$G(t) = \frac{\tau_1 \tau_2}{\tau_1 - \tau_2} (e^{-t/\tau_1} - e^{-t/\tau_2}), \quad (12.14)$$

with time to peak given by

$$t_{peak} = \frac{\tau_1 \tau_2}{\tau_1 - \tau_2} \ln\left(\frac{\tau_1}{\tau_2}\right). \quad (12.15)$$

When  $\tau_1 = \tau_2$ , the dual exponential form takes the form of an alpha function:

$$G(t) = te^{-t/\tau}, \quad (12.16)$$

where  $t = \tau_1 = \tau_2$ . In this case  $t_{peak} = \tau$ .

To calculate synaptic conductance at every time step, the second-order system is described by two first-order equations:

$$\dot{z} = -\frac{1}{\tau_1} z + x(t) \quad (12.17)$$

$$\dot{G} = -\frac{1}{\tau_2} G + z. \quad (12.18)$$

These equations can then be numerically integrated to yield  $G(t)$ . The net conductance can then be calculated by

$$\hat{g}(t) = \frac{g_{max}}{G_{peak}} G(t) w(t), \quad (12.19)$$

where  $g_{max}$  is the maximal possible synaptic conductance as determined by the modeler and  $w(t)$  is the synaptic weight.

## Appendix C: Numerical Methods

GENESIS users may select from a number of different numerical methods based on their specific simulation needs. As discussed in greater detail in chapter 14 of this volume, the choice of numerical method is critical for the fast and accurate solution of the differential equations that make up any neural simulation. Given the importance of this issue, we will briefly describe the methods available to GENESIS users. The models described in this chapter made use of the exponential Euler (network model) and backward Euler (single-cell simulations) methods.

### Explicit Methods

**Forward Euler** The forward Euler method is the simplest numerical method for approximating solutions to differential equations of the form

$$\frac{dy}{dt} = f(t). \quad (12.20)$$

At time  $\Delta t$ , we can approximate  $y(t + \Delta t)$  with

$$y(t + \Delta t) = y(t) + f(t)\Delta t. \quad (12.21)$$

Although forward Euler method allows for quick calculation at each time step, it is very unstable and therefore requires very small time steps for accurate results, which makes it quite unsuitable for most neural simulations.

**Adams-Basforth** Adams-Basforth methods, although more accurate than forward Euler, are still relatively unstable. These methods take the form

$$y(t + \Delta t) = y(t) + \Delta t(a_0 f(t) + a_1 f(t - \Delta t) + a_2 f(t - 2\Delta t) + \dots + a_n f(t - n\Delta t)), \quad (12.22)$$

where  $a_n$  coefficients may be found by expanding  $f(t - n\Delta t)$  in a Taylor series. An Adams-Basforth method is said to be of the  $(n+1)$ th order when  $f(t)$  is evaluated at  $n$  previous time steps. GENESIS allows users to choose from second- to fifth-order Adams-Basforth methods.

**Exponential Euler** This method is applicable in the case of neural simulations because the differential equations used in neural simulations (e.g., eqs. 12.5 and 12.7) are generally of the form

$$\frac{dy}{dt} = A - By. \quad (12.23)$$

In which case, we can approximate a solution at time  $t + \Delta t$  with

$$y(t + \Delta t) = y(t)e^{-B\Delta t} + \frac{A}{B}(1 - e^{-B\Delta t}) \quad (12.24)$$

Although, under most circumstances,  $A$  and  $B$  are not constants, if they change little over the course of a time step, this method gives a reasonable approximation. For simulations where neurons consist of only a few compartments and active channels, this method appears to work better than the two previously mentioned.

### Implicit Methods

Although implicit methods tend to have greater accuracy for a given time step size than explicit methods, because they are dependent on the value of  $f(t + \Delta t)$ , the solution process is more complex and thus the computational cost per time step is greater. In general, the greater accuracy permits the use of a much larger time step, leading to greater computational efficiency with implicit methods. Two implicit methods are available to GENESIS users.

**Backward Euler** Backward Euler is identical in form to forward Euler, except that  $y(t + \Delta t)$  is defined implicitly as

$$y(t + \Delta t) = y(t) + f(t + \Delta t)\Delta t. \quad (12.25)$$

This method is first-order correct in  $\Delta t$  and always stable.

**Crank-Nicholson** The Crank-Nicholson method averages forward and backward Euler methods to achieve a partial cancellation of errors. The method has the following form:

$$y(t + \Delta t) = y(t) + \frac{(f(t) + f(t + \Delta t))\Delta t}{2}. \quad (12.26)$$

This method is second-order correct in  $\Delta t$  and is usually stable except for very small  $\Delta t$ .

**Hines Method for Solving Branched Dendritic Trees** For single-cell simulations, GENESIS uses a method developed by Michael Hines (1984) to number compartments in a branched dendritic tree in such a way that they can be organized into a tridiagonal matrix, where each row represents the difference equation for the membrane potential in a compartment. This greatly facilitates the use of implicit methods because the matrix represents a series of coupled equations that can easily be solved by Gaussian elimination. (For a more detailed discussion of the Hines method and numerical methods in general, see chapter 14, this volume.)

### Appendix D: Network Connections

As we have stressed many times throughout this chapter, realistic neural models can easily exceed available computer power. For this reason, simulation systems like GENESIS seek to find simplifications that reduce computational overhead without compromising model structure too severely. In the case of network simulations, one such simplification involves representing the connections between neurons as delay lines that carry simple impulses with the duration of a single time step and a unit amplitude, which makes it unnecessary to explicitly model axonal action potentials. In GENESIS, a threshold is set in the presynaptic neuron to determine when a spike is to be transmitted to a postsynaptic cell, which receives the spike at a fixed time delay determined by the delay line. The spike is then converted into a synaptic conductance at the postsynaptic neuron. Numerous GENESIS commands exist to specify connectivity patterns, delay distributions, strength of interneuronal connections, and so on (see Bower and Beeman 1995 for further details).

### Appendix E: Additional Features of GENESIS

#### Simulating Synaptic Plasticity

GENESIS simulations can also include the effects of synaptic plasticity using the *hebbsynchan* object, which works exactly like the standard synaptic object, except that the weight value of the synapses are adjusted based on a product of the pre- and postsynaptic activities. The presynaptic activity measure is

calculated by having each spike generate an alpha-function waveform with a slow time constant (representing NMDA kinetics, which are much slower than AMPA kinetics). These alpha-functions do not directly control the channel conductance; they are only summed to generate the presynaptic activity measure. The postsynaptic activity measure is simply a low-pass-filtered version of the postsynaptic membrane potential. The time constants of this filtering and of the presynaptic alpha-function waveform are adjustable parameters of the object. Synaptic weights increase when pre- and postsynaptic activities are above user-defined thresholds and decrease when one of the activities is below its threshold. When both activities are below threshold, no change in weights occurs. Arbitrary weight change algorithms can be incorporated into this object by making minor modifications to the object's C code.

Although this object is a tremendous simplification of the complex electrical and biochemical events that underlie processes like long-term potentiation (LTP), computational efficiency in network modeling often requires that such processes be modeled as simply as possible.

### Parameter Search Routines

One of the most tedious aspects of constructing realistic models is searching through large parameter spaces to find models that produce outputs matching experimental data. GENESIS contains a library of parameter search routines that can automate this process to a large degree, in some cases reducing months of painstaking manual searches to a few days of automated searching. Several different parameter search methods have been implemented thus far, including conjugate gradient descent, stochastic search, genetic algorithms, and a continuous version of simulated annealing. (For a comparison of these methods on some simple models, see Vanier and Bower 1996.) These methods are most useful in two cases: (1) for fine-tuning a model that already generates output qualitatively similar to that of the real system, and (2) for determining whether a reasonable match to data is possible, given the model. Case 2 is especially important in that it can suggest that the model is insufficiently detailed to capture the behavior of the real system, and may suggest how it might be extended to better match the data.

### Parallel GENESIS

Parallel GENESIS was developed by Nigel Goddard and Greg Hood (1997) of the Pittsburgh Supercomputing Center to allow GENESIS to run on any platform that supports Parallel Virtual Machine (PVM), a software package developed to allow the computing resources of multiple workstations and PCs to be pooled together and used like a parallel machine. Parallel GENESIS can therefore be run on everything from multiple PCs running Linux to a CRAY supercomputer.

Certain problems in computational neuroscience are particularly well suited to parallel implementations. Parameter searches often require running a single simulation hundreds or even thousands of times while varying individual parameters. By farming out individual simulation runs to different processors, the user can perform searches that would have taken an unbearably long time on a serial machine. Similarly, large networks can be implemented in such a way that individual neurons or groups of neurons can be simulated on single processors. Parallel GENESIS commands have been tailored to facilitate these two applications.

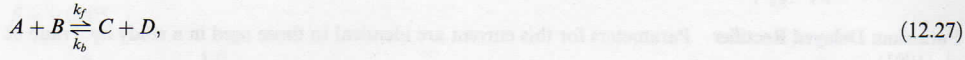
### Chemical Kinetics

In general, electrical signals in the nervous system are mediated by four mechanisms: (1) gap junctions, (2) voltage-gated channels, (3) ligand-gated channels, and (4) metabotropic receptors. Almost all of the neural models of the past decade have focused on the first three of these mechanisms, with special emphasis on the second and third, although increasing experimental evidence shows that metabotropic receptors play a major role in neural computation. These receptors are activated by an extracellular molecule (typically, a neurotransmitter or neuromodulator), which then triggers a biochemical cascade inside the neuron. This cascade then generates molecules (typically, activated G-proteins or cyclic nucleotides), which activate channels by binding to intracellular sites.

Biochemical pathways are additionally important in neural computation because they are at the root of the synaptic plasticity observed in the nervous system. The pathways underlying long-term potentiation

(LTP) are controlled by multiple factors, which makes the use of a kinetic modeling system ideal for the study of this phenomenon.

For these reasons, Upinder Bhalla (1997) developed a GENESIS library for the simulation of biochemical pathways. Simulation of biochemical reactions requires that one formulate a rate equation. If we have a reaction



where  $A$ ,  $B$ ,  $C$ , and  $D$  are biologically important molecules,  $k_f$  the forward rate constant, and  $k_b$  the backward rate constant, we can describe this with the differential equation

$$\frac{d[A]}{dt} = k_b[C][D] - k_f[A][B]. \quad (12.28)$$

Parameters such as  $k_f$  and  $k_b$  can be approximated from data found in the literature. (For a more detailed discussion of the issues and methodologies involved in the modeling of biochemical pathways, see Bower and Beeman (1997).)

## Appendix F: Model Parameters

### Parameters for Full and Reduced Single-Cell Models

Both full and reduced models use the same voltage-gated and synaptic currents. The voltage-gated currents are described using the Hodgkin-Huxley formalism set forth in “Voltage- and Calcium-Gated Currents,” chapter appendix B, and synaptic currents are parameterized according to the equations in “Synaptic Currents,” chapter appendix B. (For a more detailed justification of the parameters shown here, see Protopapas and Bower 1998b.) For all of the following equations, time is in milliseconds and membrane potential is in millivolts.

**Fast Sodium Current** Parameters for this current were obtained from a study by Traub et al. (1991). Slight modifications were made to conform to experimental data.

$$I = m^2 h \bar{g}(E_{rev} - V_m), \quad E_{rev} = 55 \text{ mV}; \quad (12.29)$$

for  $m_\infty$  and  $\tau_m$ :

$$\alpha = \frac{0.32(36.2 + V)}{1.0 - \exp\left(\frac{36.2 + V}{-4.0}\right)}, \quad \beta = \frac{0.28(9.2 + V)}{\exp\left(\frac{9.2 + V}{5.0}\right) - 1.0}; \quad (12.30)$$

for  $h_\infty$  and  $\tau_h$ :

$$\alpha = 0.128 \exp\left(\frac{32.3 + V}{-18.0}\right), \quad \beta = \frac{4.0}{1.0 + \exp\left(\frac{9.3 + V}{-5.0}\right)}; \quad (12.31)$$

**Persistent Sodium Current** Although there has been no direct evidence for the presence of this current in piriform pyramidal cells, it is known to exist in pyramidal neurons from other areas (French et al. 1990) and when added to our model, it greatly improved active behavior. Kinetic parameters come from a model by McCormick and Huguenard (1992) with the activation curve shifted slightly to the right to match experimental data from piriform cortex.

$$I = m \bar{g}(E_{rev} - V_m), \quad E_{rev} = 55 \text{ mV}; \quad (12.32)$$

for  $m_\infty$  and  $\tau_m$  (no inactivation):

$$\alpha = \frac{0.091(V + 48.0)}{1.0 - \exp\left(\frac{-(V+48.0)}{5.0}\right)}, \quad \beta = \frac{-0.062(V + 48.0)}{1.0 - \exp\left(\frac{-(V+48.0)}{5.0}\right)} \quad (12.33)$$

$$m_\infty = \frac{1.0}{1.0 + \exp\left(\frac{(43.0+V)}{-5.0}\right)}, \quad \tau_m = \frac{1.0}{\alpha + \beta} \quad (12.34)$$

**Potassium Delayed Rectifier** Parameters for this current are identical to those used in a study by Traub et al. (1991).

$$I = m\bar{g}(E_{rev} - V_m), \quad E_{rev} = -90 \text{ mV}; \quad (12.35)$$

for  $m_\infty$  and  $\tau_m$  (no inactivation):

$$\alpha = \frac{0.016(-39.2 - V)}{\exp\left(\frac{-39.2-V}{5.0}\right) - 1.0}, \quad \beta = 0.25 \exp\left(\frac{-54.3 - V}{40.0}\right) \quad (12.36)$$

**Potassium A-Current** This current has been studied experimentally by Banks, Haberly, and Jackson (1996) in piriform pyramidal neurons. We use the parameters obtained in that study.

$$I = m^3 h \bar{g}(E_{rev} - V_m), \quad E_{rev} = -90 \text{ mV}; \quad (12.37)$$

for  $m_\infty$  and  $\tau_m$ :

$$\alpha = 0.5 \exp\left(\frac{0.5V + 19.65}{15.4}\right), \quad \beta = 0.5 \exp\left(\frac{0.5V + 19.65}{-15.4}\right); \quad (12.38)$$

for  $h_\infty$  and  $\tau_h$ :

$$\alpha = 0.04 \exp\left(\frac{0.9V + 59.13}{-6.86}\right), \quad \beta = 0.04 \exp\left(\frac{0.1V + 6.57}{6.86}\right) \quad (12.39)$$

**Potassium M-Current** Although there is experimental evidence for the existence of the M-current in piriform pyramidal neurons (Constanti and Galvan 1983a; Constanti and Sim 1987a, 1987b), its exact parameters have not been well described. Therefore, we use an M-current much like the one described by Yamada, Koch, and Adams (see chapter 4, this volume) except that the kinetics are approximately three times as fast. This current does not inactivate.

$$I = m\bar{g}(E_{rev} - V_m), \quad E_{rev} = -96 \text{ mV} \quad (12.40)$$

$$m_\infty = \frac{1.0}{1.0 + \exp\left(\frac{(35.0+V)}{-10.0}\right)} \quad (12.41)$$

$$\tau_m = \frac{330.0}{11.3(\exp\left(\frac{V+35.0}{20.0}\right) + \exp\left(\frac{V+35.0}{-10.0}\right))} + 10.89 \quad (12.42)$$

**Potassium Slow AHP Current** Voltage clamp and pharmacological evidence support the existence of a slow AHP current in piriform pyramidal neurons (Constanti and Sim 1987a). Because the precise kinetics and calcium dynamics underlying this current are not well described, we constructed a phenomenological model based on the best fit we could obtain with the simple calcium dynamics described in equation 6.1. We use the Hodgkin-Huxley formalism to model this calcium-dependent current, except that the voltage-dependent gate  $m$  is replaced by the calcium-dependent gate  $z$  as follows. All concentrations are in micromolar and times are in milliseconds.

$$I = z\bar{g}(E_{rev} - V_m), \quad E_{rev} = -96 \text{ mV} \quad (12.43)$$

$$\frac{\partial z}{\partial t} = \frac{z_\infty - z}{\tau_z} \quad (12.44)$$

$$\alpha = \min\left(\frac{[\text{Ca}^{2+}]}{0.52 \mu\text{M}}, 0.01\right) \quad (12.45)$$

$$\beta = 0.0005 \quad (12.46)$$

$$z_\infty = \frac{\alpha}{\alpha + \beta}, \quad \tau_z = \frac{1.0}{\alpha + \beta}. \quad (12.47)$$

**Fast Calcium Current** Although a voltage-gated calcium current has been observed in piriform pyramidal neurons (Constanti et al. 1985), it has not been parameterized, nor have there been any efforts to determine the individual calcium currents that may underlie the more general voltage-gated calcium current observed by Constanti et al. (1985). Therefore, we constructed a phenomenological model of the voltage clamp data obtained for the calcium current in the study by Constanti et al. (1985). To accurately replicate the voltage clamp data, we found it necessary to use two calcium current components, one fast, and one slow. Because of the enormous calcium concentration gradient that exists across the membrane, it is not possible to use the standard Hodgkin-Huxley model of voltage-gated currents; instead, we must utilize the Goldman-Hodgkin-Katz equation (discussed in greater detail in chapters 4, 5, and 6, this volume). This equation calculates transmembrane current and is dependent on a variable representing the  $\text{Ca}^{2+}$  permeability of the membrane. We use the gating concept from the Hodgkin-Huxley model to develop an expression for calcium permeability due to the fast calcium current:

$$I = I_{CaF} = P_{CaF} z_{Ca}^2 \frac{VF^2}{RT} \frac{[\text{Ca}^{2+}]_i - [\text{Ca}^{2+}]_o \exp\left(-\frac{z_{Ca} FV}{RT}\right)}{1.0 - \exp\left(-\frac{z_{Ca} FV}{RT}\right)}, \quad (12.48)$$

where  $P_{CaF}$  is the  $\text{Ca}^{2+}$  permeability due to the fast calcium current,  $z_{Ca}$  is the valency of the calcium ion, and  $V$ ,  $R$ ,  $F$ , and  $T$  are the membrane potential, gas constant, Faraday constant, and temperature (in Kelvins), respectively. To calculate permeability, we use the following expression:

$$P_{CaF} = m^2 h \bar{P}, \quad (12.49)$$

where  $m$  and  $h$  are activation and inactivation gates, as before, and  $\bar{P}$  the maximum permeability due to the fast calcium current.

$$m_\infty = \frac{1.0}{1.0 + \exp\left(\frac{42.0 + V}{-2.0}\right)} \quad (12.50)$$

$$\tau_m = \frac{1.0}{\exp\left(\frac{162.0 + V}{-26.7}\right) + \exp\left(\frac{26.8 + V}{18.2}\right)} + 1.0 \quad (12.51)$$

$$h_\infty = \frac{1.0}{1.0 + \exp\left(\frac{54.0 + V}{2.0}\right)} \quad (12.52)$$

$$\tau_h = \frac{18.0}{\exp\left(\frac{82.0 + V}{-2.7}\right) + \exp\left(\frac{28.0 + V}{28.0}\right)} + 3.0 \quad (12.53)$$

**Slow Calcium Current** The slow component of the calcium current is described by the following equation:

$$P_{CaS} = mh \bar{P} \quad (12.54)$$

$$m_\infty = \frac{1.0}{1.0 + \exp\left(\frac{32.0 + V}{-10.0}\right)} \quad (12.55)$$

**Table 12.2**

Synaptic channel parameters for full and reduced models of piriform cortex pyramidal cell

Type	Location	$\tau_1$	$\tau_2$	$E_{rev}$
Non-NMDA (excitatory)	Ia, Ib	1.50 msec	3.00 msec	0.0 mV
NMDA	Ia, Ib	(see text)		0.0 mV
GABA <sub>A</sub>	II	1.00 msec	5.50 msec	-60 mV
GABA <sub>B</sub>	Ia	150 msec	180 msec	-90 mV

**Table 12.3**

Neuronal parameters for piriform cortex network model

$C_m$	Specific membrane capacitance	2.0 $\mu\text{F}/\text{cm}^2$				
$R_{m(p)}$	Pyramidal-specific membrane resistance	4.0 $\text{k}\Omega \cdot \text{cm}^2$				
$R_{(m(i))}$	Interneuron-specific membrane resistance	2.0 $\text{k}\Omega \cdot \text{cm}^2$				
$R_a$	Specific axial resistance	100 $\Omega \cdot \text{cm}$				
$R_e$	Extracellular resistance	100 $\Omega/\text{cm}$				
$R_{IN}$	Pyramidal input resistance	38 $\text{M}\Omega$				
$E_m$	Resting membrane potential	-70 mV				
$t_r$	Absolute refractory period	10 ms				
$t_e$	Synaptic delay	0.8 ms				
$t_{e(ff)}$	Feedforward inhibitory delay	8 ms				
Synaptic conductances						
	$\tau_1$	$\tau_2$	$g_{peak}^*$	Reversal potential		
excitatory	1 msec	3 msec	200 pS/synapse	0 mV		
GABA <sub>A</sub> (Cl <sup>-</sup> )	1 msec	7 msec	500 pS/synapse	-65 mV		
GABA <sub>B</sub> (K <sup>+</sup> )	10 msec	100 msec	50 pS/synapse	-90 mV		
Action potential conductances						
	$\tau_1$	$\tau_2$	$g_{peak-pyr}$	$g_{peak-fb}$	$g_{peak-ff}$	$E_{rev}$
Na <sup>+</sup>	0.2 msec	0.2 msec	450 nS	75 nS	35 nS	55 mV
K <sup>+</sup>	1.0 msec	1.0 msec	50 nS	8 nS	4 nS	-90 mV
Cellular dimensions						
		Length	Diameter			
Pyramidal soma		70 $\mu\text{m}$	20 $\mu\text{m}$			
Pyramidal dendrites (4)		120 $\mu\text{m}$	4 $\mu\text{m}$			
Feedforward interneuron soma		10 $\mu\text{m}$	10 $\mu\text{m}$			
Feedback interneuron soma		15 $\mu\text{m}$	15 $\mu\text{m}$			

**Table 12.4**

Connection parameters for piriform cortex network model

Pathway velocities	
Main afferent LOT	7.00 m/sec (SD = 0.06, max/min = 7.20/6.80)
Afferent collateral	1.60 m/sec (SD = 0.06, max/min = 1.80/1.40)
Rostrally directed	0.85 m/sec (SD = 0.13, max/min = 1.25/0.45)
Caudally directed	0.37 m/sec (SD = 0.03, max/min = 0.48/0.25)
Inhibitory pathways	1.00 m/sec (SD = 0.06, max/min = 0.80/1.20)
Pathway extents	
Local pyramidal to pyramidal	0.5 mm
Distant pyramidal to pyramidal	10.0 mm
Pyramidal to feedback interneuron	2.0 mm
Pyramidal to feedforward interneuron	0.5 mm
Feedback interneuron to pyramidal	1.0 mm
Feedforward interneuron to pyramidal	1.0 mm
Pathway space constants	
Pyramidal to pyramidal	5 mm
Pyramidal to interneurons	5 mm
Interneurons to pyramidal	5 mm
Main LOT	20 mm
LOT collaterals	10 mm
Connection probabilities	
LOT to pyramidal/interneurons	0.10
Local pyramidal to pyramidal	0.20
Distant pyramidal to pyramidal	0.02
Pyramidal to interneurons	0.20
Interneurons to pyramidal	1.00
Synapses onto pyramidal cells	
From LOT	1,500
From local pyramidal	750
From distant caudal pyramidal	1,200
From distant rostral pyramidal	2,200
From feedback interneurons	1,500
From feedforward interneurons	500
Synapses onto feedback interneurons	
From LOT	50
From pyramidal	300
Synapses onto feedforward interneurons	
From LOT	130
From pyramidal	50

$$\tau_m = \frac{1.0}{\exp(\frac{3.2+\nu}{-6.7}) + \exp(\frac{16.8+\nu}{18.2})} + 3.0 \quad (12.56)$$

$$h_\infty = \frac{1.0}{1.0 + \exp(\frac{40.0+\nu}{35.0})} \quad (12.57)$$

$$\tau_h = \frac{350.0}{\exp(\frac{35.0+\nu}{12.0}) + \exp(\frac{25.0+\nu}{-12.0})} + 10.0. \quad (12.58)$$

**Synaptic Currents** Table 12.2 lists the parameters for the synaptic currents in the single-cell models that were described by the dual exponential form (see “Synaptic Currents,” chapter appendix B; the Holmes-Levy 1990 model of NMDA conductance is described in chapter 6, this volume).

### Parameters for the Piriform Cortex Network Model

Tables 12.3 and 12.4 list all of the parameters for the network model. The “space constants” referred to in table 12.4 show the space constant for the exponential decay in connection strength along different synaptic pathways.